ELSEVIER

Journal of Power Sources 91 (2000) 161–171

JOURNAL OF POWER SOURCES

www.elsevier.com/locate/jpowsour

Effect of various stack parameters on temperature rise in molten carbonate fuel cell stack operation

Joon-Ho Koh *, Byoung Sam Kang, Hee Chun Lim

Power Generation Laboratory, Korea Electric Power Research Institute, 103-16 Munji-dong, Yusong-ku, Taejon 305-380, South Korea

Received 14 January 2000; accepted 29 February 2000

Abstract

A mathematical stack model is used to predict the temperature at a constant-load operation of molten-carbonate fuel cell stacks. The validity of the model is proved by a comparison with measured temperature data obtained from the operation of a 5-kW test stack. The model is applied extensively for the simulation of temperature profiles in a larger stack to analyze the effect of various stack parameters on temperature rise and cooling. The results verify that the cathode gas flow has a predominant effect on the maximum temperature inside the stack while the inlet and heating temperatures have limited influence. This explains the need for pressurized operations for control of stack temperature. © 2000 Elsevier Science B.V. All rights reserved.

Keywords: MCFC, molten carbonate fuel cell; Stack model; Temperature distribution; Cooling

1. Introduction

Fuel cells produce a significant amount of thermal energy as well as electrical power, because the electrochemical reactions cannot convert the change of internal energy completely into electricity. A temperature rise is inevitable during the operation of fuel cell stacks. The temperature range allowed for stable cell performance depends upon the type of fuel cell. In the case of a molten-carbonate fuel cell (MCFC), the normal operating temperature is 650°C and the allowable temperature variation is the range of 600 to 700°C [1]. At a temperature lower than 600°C, the cell performance drops significantly, while a temperature higher than 700°C accelerates material corrosion. Compared with other fuel cells with relatively nonreactive electrolytes such as ceramic oxide or polymer membrane, the use of carbonate salt in MCFC creates a chemically active environment on the contact surface of the cell components even at the normal operation temperature. To guarantee a stable performance during the commercially targeted operation period (~ 40 000 h per stack), the inside stack temperature should be controlled within the specified range.

Stack temperature control in MCFC can be achieved in two ways. One is a direct or indirect internal reforming stack where the endothermic reforming reactions absorb heat generated from cells and lead to a thermal balancing state so that the maximum temperature does not exceed the allowable limit [2]. The other way of temperature control is cooling with an excess amount of process gas, (compressed air to cathode) which lowers the stack temperature by convective heat transfer. In the latter, which has been sought for external-reforming MCFC stacks, an increase of inlet pressure might be a limiting factor though this problem can be solved by pressurized stack operation. A choice between internal and external reforming methods will be made on an economic basis, and each has its own merits and drawbacks. Pressurized operation is desired in the case of air-cooled MCFC stacks not only to reduce the pressure drop of gas streams but also to obtain a higher cell performance at elevated pressures [3,4]. Some MCFC developers are interested in pressurized MCFC stacks for this reason.

Past studies demonstrated valid stack models for prediction of temperature and other variables in MCFCs [5–8]. This study uses an MCFC stack model similar to others,

* Corresponding author. Tel.: +82-42-865-5393; fax: +82-42-865-5374.

E-mail address: koh@kepri.re.kr (J.-H Koh).

0378-7753/00/$ - see front matter
PII: S0378-7753(00)00463-8

but attempts to show various aspects of the stack temperature rise during a large-area MCFC stack operation from numerical simulations under several different operating conditions. The aim is to draw a conclusion that systematically explains how the stack temperature can be managed efficiently in an external reforming MCFC stack, especially one with co-flow internal manifolds. The characteristics of a large-area stack should be verified in as much detail as possible, but it is not cost-effective to build and test such a large stack for fundamental research purposes. That kind of task can be easily done when mathematical models are utilized for the simulation of stack operation, as demonstrated in this paper.

2. Mathematical model for MCFC stack

The MCFC stack considered in this study was a planar stack with vertically piled cells and internal gas manifolds. The side and top cross-section areas of this type of stack are shown in Fig. 1. The electrochemically active zone is the cell area represented by $L \times W$. The size of separator plates is larger than the electrochemical reaction zone so as to include gas manifolds at the inlet and outlet zones. The area of separator plates outside the electrochemical reaction zone is the wet seal, which plays an important role in preventing fuel and oxidant gas streams from leaking. The sealing of the wet seal is achieved with a liquid carbonate melt filled in a porous matrix plate between a pair of separator plates. At the same time, the wet seal is a weak point of the MCFC because corrosive attack of carbonate salt occurs mostly in this area.

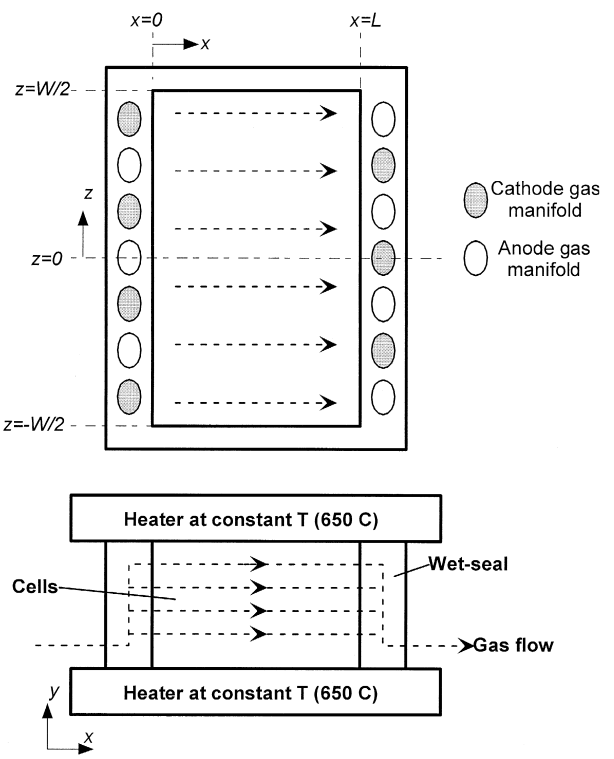

Fig. 1. Schematic views of co-flow MCFC stack.

Mathematical models were derived for a stack which had the effective cell area shown in Fig. 1. The wet seal area is excluded in the model formulation, but it is accounted for in stack boundary conditions. The governing equations are built for transport variables based on continuum mechanics at a steady state and the cell performance variables. The equations are expressed in Cartesian coordinates with x as an axial distance, y as a vertical distance, and z as a transverse distance. Each cell is physically composed of a pair of electrodes (cathode and anode) and an electrolyte-filled matrix layer between them, but they are treated as a single layer with electrochemical reactions taking place homogeneously.

The conservation equation for heat transfer with consumption and generation of thermal energy is expressed as:

$$\nabla \cdot \rho \underline{u} C_p T = \nabla \cdot (k \nabla T) + \Sigma Q \tag{1}$$

where Q represents a heat source or sink due to cell reactions or gas-phase reactions. The heat generated from cell reactions is obtained from the enthalpy change of an overall cell reaction minus the electrical power produced, i.e.,

$$H_2 + \frac{1}{2}O_2 \rightarrow H_2O + \text{electricity} + \text{heat}$$

$$\Delta H_{f,H_2O} = -(240\,506 + 7.3835T) \qquad [\text{J/mol}] \tag{2}$$

$$Q_{\text{cell}} = \left\{\left(-\Delta H_{f,H_2O}\right) r_{j,\text{cell}} - iV_{\text{cell}}\right\} \frac{1}{\delta_{\text{cell}}} \tag{3}$$

where $r_{j,\text{cell}}$ is the number of reactant moles per unit surface area for species j and is obtained from Faraday's equation if current density, i, is given by

$$r_{j,\text{cell}} = \frac{i}{z_j F} \tag{4}$$

Besides the cell reaction, there is an additional heat source or sink from an anode gas reaction called the water–gas-shift reaction. The enthalpy change of this reaction is, however, usually negligible compared with that of the cell reaction, i.e.,

$$CO + H_2O \leftrightarrow H_2 + CO_2$$

$$-Q_{\text{shift}} = \Delta H_{\text{shift}} = -43\,729 + 9.4657T \qquad [\text{J/mol}] \tag{5}$$

A set of momentum conservation equations was also included to calculate pressure fields and velocity distribution:

$$\nabla \cdot \rho \underline{u} = \pm m_{CO_3^{2-}} \quad (6)$$

$$\nabla \cdot \rho \underline{u}\underline{u} = \nabla \cdot (\mu \nabla \underline{u}) - \nabla P \quad (7)$$

Eqs. (6) and (7) apply for the gas streams of the anode and the cathode which are not supposed to be mixed unless a local cell breakage occurs (cross-over). Since a hydrogen molecule in the anode gas reacts with a carbonate ion supplied from the electrolyte layer though ionic conduction, the anode gas stream acquires a mole of carbonate for each hydrogen molecule consumed. The result is that a total mass increases by a net amount equal to the mass of carbonate. The reverse is true for the cathode where a carbonate ion is created as a result of reaction of carbon dioxide and oxygen. Therefore, there is an overall mass increase in the anode gas (positive source in Eq. (6)) and an overall mass decrease in the cathode gas (negative source in Eq. (6)).

$$H_2 + CO_3^{2-} \rightarrow CO_2 + H_2O + 2e^- \quad \text{(anode)}$$

$$CO_2 + \frac{1}{2}O_2 + 2e^- \rightarrow CO_3^{2-} \quad \text{(cathode)}$$

While an overall mass conservation is expressed as in Eq. (6), the conservation of each species is obtained from differential mass balance equations with a variety of source and sink terms such as electrochemical reactions. Written in terms of molar concentration, C_j, the mass balance equations are generally expressed as:

$$\nabla \cdot \underline{u} C_j = \nabla \cdot (D \nabla C_j) + \Sigma r_j \quad (8)$$

If only one-dimensional axial variation of concentration is considered to be predominant and a diffusion contribution in the bulk gas streams is ignored, then the equation is expressed in the following simple form:

$$\frac{\mathrm{d}(u_x y_j C)}{\mathrm{d}x} = \frac{i}{z_j F}\frac{1}{\delta_g} \quad (\text{for species } j) \quad (9)$$

where δ_g denotes a gas channel depth and is required to convert a surface flux into a volumetric flux. In this mass balance equation, diffusion terms are ignored because the rate of molecular diffusion in bulk gas streams is very small compared with the convection mass transfer rate. The concentration variation in the *y*-direction is also neglected. The right-hand side is the rate of species consumed or generated from the cell reactions according to Faraday's law (Eq. (4)).

If we assume a uniform current density (i) over the electrode plane surface, Eq. (9) becomes an ordinary differential equation which can be solved for each species mole fraction (y_j) and a total molar flux of each gas stream ($u_x C$).

$$y_j = \frac{1}{u_x C}\left((u_x C y_j)_{\text{in}} + \frac{i}{z_j F \delta_g} x \right) \quad (10)$$

$$u_x C = (u_x C)_{in} + \sum_j \frac{i}{z_j F \delta_g} x \quad (11)$$

The water–gas-shift reaction equilibrium is assumed at the inlet feed anode gas mixture.

$$\frac{y_{H_2} y_{CO_2}}{y_{H_2O} y_{CO}} = \frac{P_{H_2} P_{CO_2}}{P_{H_2O} P_{CO}} = K_{\text{shift}} \quad (12)$$

$$K_{\text{shift}} = 157.02 - 0.4447T + 4.2777 \times 10^{-4} T^2 - 1.3871 \times 10^{-7} T^3 \quad (13)$$

In fuel cell reactions, the rate of reaction is related to a local current density, as Eq. (4) or (9) show. The local current density is affected by temperature and reactant partial pressures, and is therefore coupled with other model equations. A precise analysis of current density distribution requires electrochemical kinetics in microscale dimensions and includes pore diffusion and reaction at three-phase boundaries (gas reactant + electrolyte + electrode surface). For simplicity, we assume the total current load is uniformly distributed in the cell plane.

A reversible cell potential is calculated from a set of thermodynamic equation and equilibrium data, i.e.,

$$E_{\text{eq}} = E^0 + \frac{RT}{2F} \ln\left[\frac{P_{H_2,a}\sqrt{P_{O_2,c}}}{P_{H_2O,a}} \frac{P_{CO_2,c}}{P_{CO_2,a}} \right] \quad (14)$$

$$E^0 = 1.2723 - 2.7645 \times 10^{-4} T \quad (15)$$

The cell performance is obtained from a reversible cell potential and irreversible losses due to internal resistance and polarization.

$$V_{\text{cell}} = E_{\text{eq}} - i(R_{\text{ohm}} + \eta_{\text{anode}} + \eta_{\text{cathode}}) \quad (16)$$

Internal cell resistance is usually expressed by means of an Arrhenius equation as a function of temperature. Correlations for polarization losses were obtained from Ref. [9].

$$R_{\text{ohm}} = 0.5 \times 10^{-4} \exp\left[3016 \left(\frac{1}{T} - \frac{1}{923} \right) \right] \quad (17)$$

$$\eta_{\text{anode}} = 2.27 \times 10^{-9} \exp\left(\frac{6435}{T} \right) P_{H_2}^{-0.42} P_{CO_2}^{-0.17} P_{H_2O}^{-1.0} \quad (18)$$

$$\eta_{\text{cathode}} = 7.505 \times 10^{-10} \exp\left(\frac{9298}{T} \right) P_{O_2}^{-0.43} P_{CO_2}^{-0.09} \quad (19)$$

The proposed mathematical model is solved using one of the commercially available computational fluid dynamics solvers, PHOENICS (version 2.2) on PC. Eq. (1) was applied for cell, separator, and gas streams to obtain temperature fields, and Eqs. (6) and (7) were solved for pressure fields [10]. The concentration variation after the water–gas-shift equilibrium at the anode inlet was directly obtained from Eqs. (10) and (11) for a given average current density and was implemented in the computation program. Eqs. (14)–(19) were also implemented in the user-subroutine program to obtain cell voltage as a function of temperature and reactant partial pressures. The thermal and transport properties of gases were estimated from correlations for ideal gas [11]. Solid thermal properties were extracted from literature [12]. The simulation was conducted for a 20-cell MCFC stack of 3000-cm^2 cell area for model validation and a 40-cell stack of 6000-cm^2 cell area for an extensive study of temperature distribution in the MCFC.

3. Test of stack performance and temperature

A 20-cell MCFC stack was constructed with an external reformer for hydrogen supply and gas preheating units. The cells were made with a Ni–Cr alloy for the anode, lithiated nickel oxide for the cathode, a molten carbonate mixture (Li_2CO_3/K_2CO_3) for the electrolyte, and a ceramic matrix (Υ-$LiAlO_2$) for the electrolyte support. These are a set of the most widely used component materials at the present time. The length of each cell is 41 cm and the width is 76 cm. The separator plates are 60×82 cm. The height of the stack with 20 cells was approximately 35 cm. In the 21 separator plates needed for the 20 cells, the top- and bottom-end plates are 8 cm thick each and this size was needed to allow large channels for the inlet and outlet gas flow paths. The separator plates located every five cells from either the upper- or the lower-end plate are 1 cm thick, and these separator plates are designed to allow for insertion of thermocouples in order to measure inner stack temperatures during operation. The other remaining separator plates are all 0.5 cm thick, and they also act as bipolar plates between two adjacent cells. Electrical heating plates were placed on both the top- and bottom-end separators, and they maintained a constant temperature (650°C) during operation unless specified otherwise. The stack was thermally and electrically insulated from the outside.

The feed amounts of fuel and oxygen were determined from the load current and the gas utilizations. Stack performance was measured mostly at 100 and 150 mA cm^{-2} with a gas utilization rate of 0.4 to 0.6. The feed composition of the cathode gas was $O_2/N_2/CO_2 = 15/55/30$, and the feed composition of the anode gas was $H_2/CO_2/H_2O = 72/18/10$. The steam content of the anode gas was controlled via a humidifier temperature maintained at 50°C.

4. Results and discussion

4.1. Comparison with measured stack data

A set of boundary conditions for the stack is necessary to solve the proposed differential equations. For the theoretically predicted temperature distribution to match real data, the boundary conditions of temperature need to be set properly. Several sets of temperature boundary conditions were examined for the stack model and the accuracy of predictions was analyzed by comparing these conditions with temperatures measured from the 20-cell test stack. For the specified size and stack design, we obtained satisfactory temperature prediction when the wet seal temperature was reasonably assumed to account for heat transfer from the stack boundary to the surroundings. The front wet seal of the gas inlet zone was assumed to have the inlet gas temperature, and the rear wet seal temperature at the gas outlet was assumed to correspond with the heating temperature of the upper and lower heating plates. For three-dimensional simulations, the side wall temperature ($z = \pm W/2$) was assumed to vary linearly with the axial position from the front wet seal temperature to the rear wet seal. Details of such an analysis have been reported elsewhere [12]. Here, we show a typical set of temperature measurements and the results of a very reliable prediction from simulations under two different current load conditions, as given in Fig. 2. The measured temperature points and contours from the simulation are plotted in a two-dimensional cross-section of the stack (the x–y plane of Fig. 1). The temperature contours reveal that the central zone near the outlet is the hottest part of the stack. The maximum temperature at 150 mA cm^{-2} is 713°C, i.e., larger than the upper limit of the suggested operation temperature range. The inlet centre is the coldest zone. Since the coldest and hottest zones are located in the middle of the stack inlet and outlet, a one-dimensional temperature profile along the central axis will characterize temperature distribution behaviour of this co-flow type stack most effectively.

While each temperature contour line in Fig. 2 does not show a monotonous variation, especially in the vertical direction, it is explained by the different thickness of the separator plates at which it is noted that the multiple apices in Fig. 2 are observed after every five cells at which a thicker separator plate is placed for temperature measurement. The thicker separator plates will absorb more heat from cells than the other thin plates, which results in a lower local temperature. Overall, the agreement between the data and prediction is quite sufficient to ensure the

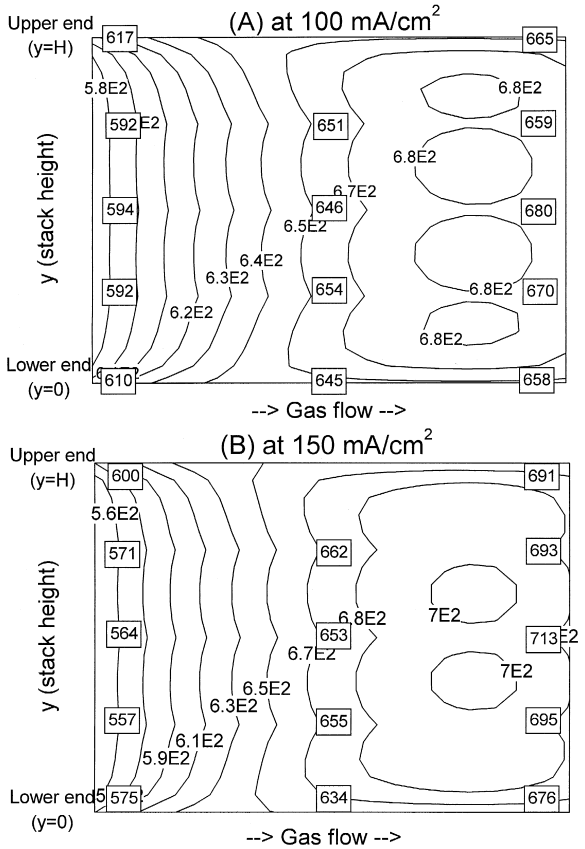

Fig. 2. Side view of temperature distributions from model and comparison with measured data from a kilowatt-scale test stack: (A) fuel and oxygen utilization = 0.4 at 100 mA cm^{-2} load with a gas inlet temperature of 550°C; (B) fuel and oxygen utilization = 0.6 at 150 mA cm^{-2} load with a gas inlet temperature of 500°C. (□) measured temperature in °C.

validity of the model and also the aforementioned temperature boundary conditions for more extensive simulations.

4.2. Effect of temperature distribution on cell performance

The temperature distribution over the area of each plane is obtained from three-dimensional simulations. The coordinates include axial (x), vertical (y), and transverse (z) directions. The x–z plane projects a whole view of each single layer of the cells and the separator plates. A view of temperature distribution in the middle of the stack height ($y = H/2$) is illustrated in Fig. 3. Only half the area (from $z = 0$ to $z = W/2$) of the entire plane is shown because a plane symmetry is assumed. The wet seal area is not included in this plot. The same type of plots were made for the predicted power density distributions in Fig. 4. The stack simulation conditions for Figs. 3 and 4 are identical to those of Fig. 2. In Figs. 2(A), 3(A) and 4(A), the feed gas inlet temperature is 550°C and the current load is 100 mA cm^{-2}. The corresponding values in Figs. 2(B), 3(B) and 4(B) are 500°C and 150 mA cm^{-2}. The lower inlet temperature in the B plots was mainly for a practical reason with respect to the operation of the test stack. The stack temperature rose above 700°C when the load current density was increased from 100 to 150 mA cm^{-2} at atmospheric pressure. Such a low inlet gas temperature at 150 mA cm^{-2} was necessary in order to manage the stack temperature within the allowable limit.

The temperatures in Fig. 3 are plotted on the same scale for both case A (100 mA cm^{-2}) and the case B (150 mA cm^{-2}) to provide a fair comparison. The same is also true for the power density curves under the two different conditions in Fig. 4. At a moderate current load (100 mA cm^{-2}), the temperature variation is mostly in the range of 550°C to 680°C, and the power density is uniform with an average value of 0.087 W cm^{-2}. At the higher load (150 mA cm^{-2}), however, the temperature variation from inlet to outlet has a very steep gradient, and the power density distribution exhibits significant deviation from the average value (0.113 W cm^{-2}). The influence of temperature variation on cell performance, even in this pilot-scale test

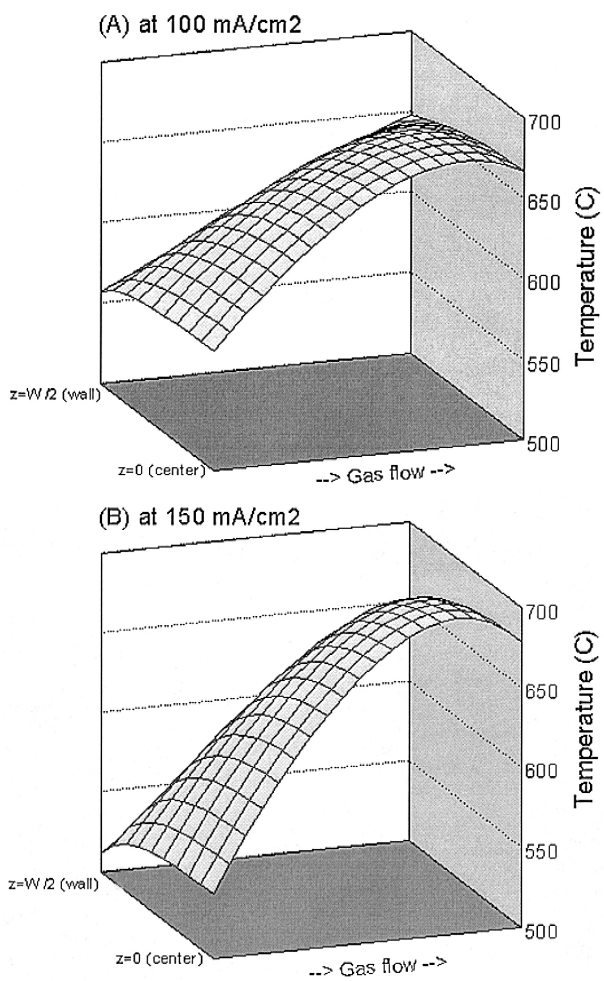

Fig. 3. Plane view of temperature distributions in middle of stack height: (A) and (B) cases are the same as those in Fig. 2.

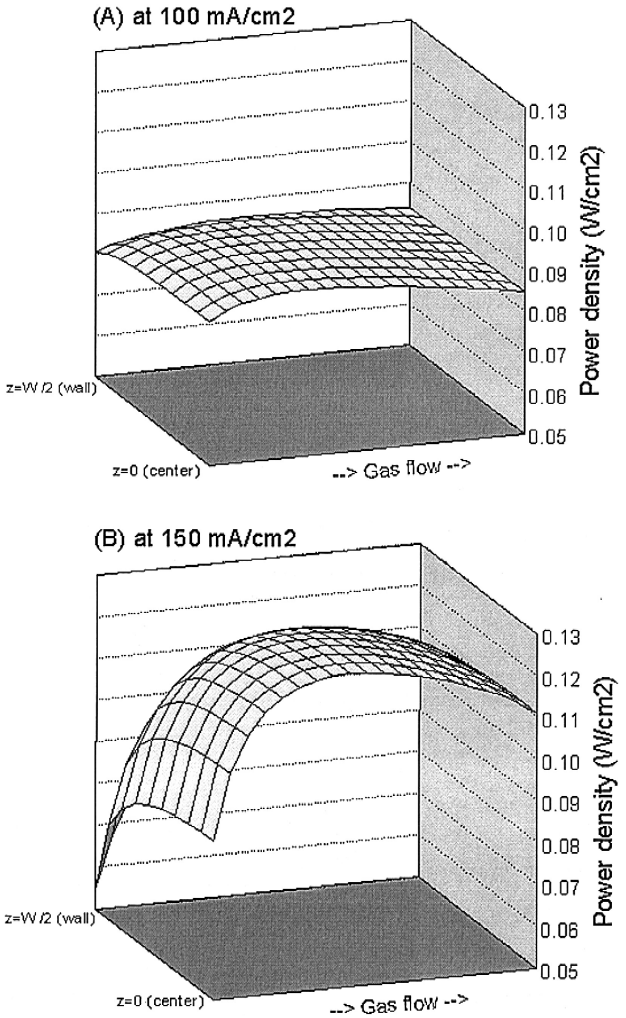

Fig. 4. Plane view of power density distributions in middle of stack height: (A) and (B) cases are the same as those in Fig. 2.

stack, is clearly demonstrated in Figs. 3 and 4. In an isothermal cell operation, which is possible only in small cells, the electrical power density will decrease from the inlet to the outlet, as influenced by anode gas partial pressures [13]. The results of Fig. 4(B) show a very low power density at the inlet, and this is due to the low temperature, as indicated in Fig. 3(B). Such a low stack temperature near the inlet is attributed to the low inlet gas temperature, but it is necessary during actual stack operation to keep the maximum stack temperature lower than 700°C as already explained. It emphasizes the importance of heat management in MCFC stack operation to achieve a stable cell performance. The power density distribution at 100 mA cm^{-2} in Fig. 4(A) is surprisingly uniform, probably because the opposite effects of two operating variables (temperature and reactant concentration) are balanced under these conditions. In other words, the axial increase of temperature that enhances cell reaction kinetics compensates for the decrease in the reactant partial pressure. The stack tested for this study was in a stable operation at 100 mA cm^{-2} for approximately 3500 h as shown in Fig. 5. We expect that degradation of the stack performance would be accelerated at a higher load, i.e, 150 mA cm^{-2}, due to a more severe temperature distribution.

4.3. Effect of cell size and numbers

As discussed above, a co-flow stack is well characterized by axial variation of performance and operation variables [14]. In the following, we show the effect of various stack parameters on the axial temperature profile, which is of primary interest in this study. The temperature profiles are for the central axis of the stack ($y = H/2$ and $z = 0$ in Fig. 1) from two-dimensional simulations. First, axial temperature profiles of stacks with different sizes are compared in Fig. 6. A 100-cm^2 cell is common in the laboratory for fundamental research, and there is no significant temperature gradient in this cell size. The maximum available cell size for commercial applications is 1 m^2 and will provide stacks of a few hundred kilowatts. Temperature profiles in stacks with three different cell areas (1000, 3000, and 6000 cm^2) are compared in Fig. 6. For two-dimensional simulations, only the cell length is required. The cell length is usually about half the cell width, and our simulation was undertaken on this basis. The matching cell length is 22 cm for 3000 cm^2, 40 cm for 3000 cm^2, and 55 cm for 6000 cm^2. Our test stack (20-cell of 3000 cm^2) had cells with a length of 41 cm. The axial temperature profiles for the three different sizes have an identical shape with increasing temperature from inlet to outlet, as shown in Fig. 6, though the temperature drops a little near the outlet. This exit temperature drop is probably due to a heat loss at the boundary. The maximum temperature rise appears to increase proportionally with cell size. The stack of 1000 cm^2 cells shows a maximum temperature well below

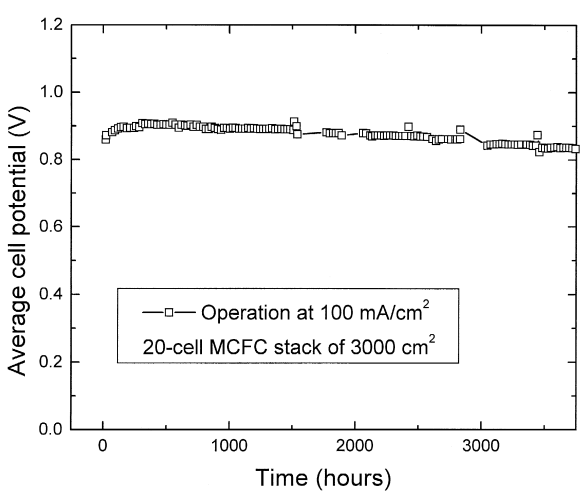

Fig. 5. Time-dependent average cell performance of kilowatt-scale MCFC test stack.

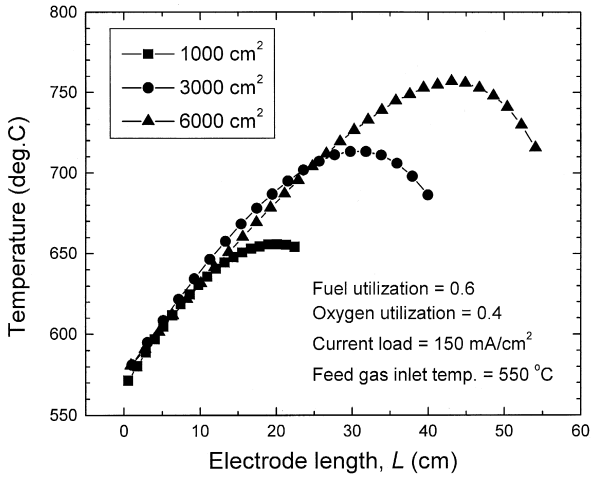

Fig. 6. Axial temperature profiles from numerical simulations for stacks of different cell sizes.

700°C. This is a very desirable operating condition, but this size of stack is too small to be used for stationary power generation purposes. The stack of 3000 cm^2 cells displays a temperature rise to about 700°C, i.e., above the upper limit for cell operation. It should be recalled (see above) that we operated the same size of test stack at a lower current load and with a lower feed gas temperature to avoid this temperature rise. The maximum temperature of 6000 cm^2 stack is higher than 750°C, far above the upper limit.

A comparison of axial temperature profiles at different stack heights, i.e., piles with different numbers of cells, is given in Fig. 7. With more cells, the upper and lower boundaries of a stack become further apart as the stack height increases. External control of stack temperature is possible at the stack boundaries by means of heating power or feed gas temperature. Stack heaters are influential only in the region close to the heating plates which are located at the upper and lower ends. The inside core of a stack is little influenced by stack heaters, but is influenced mostly by the heat of the cell reactions. The maximum temperature may therefore be controlled with stack heaters only when the stack height is very small, as the simulation shows in Fig. 7. With only five cells, the stack temperature is much lower than that with 10 or more cells. An increase in cell number from 5 to 10 results in a maximum temperature rise of more than 20°C. With an increase of 10 to 20, the temperature rise is about 10°C. After 20 cells, no significant effect is seen with adding more cells. Both the inlet and outlet temperatures of axial profiles are unchanged, and only the maximum temperature point at the apex of each temperature distribution curve moves upward as cells are added to the stack (Fig. 7).

In general, the effect of the number of cells is small compared with that of cell size. To increase the power generation capacity of a stack, both cell area and stacking cell numbers should be increased. The data in Figs. 6 and 7 indicate that the enlarged cell area is more responsible for temperature distribution than the number of cells. In the following study, we focus on the largest cell size (6000 cm^2) among those compared in Fig. 6, and conduct a parametric analysis to investigate the effect of several stack operation parameters on the axial temperature profile. In all the simulations, the gas utilization was 0.6 for fuel (anode) and 0.4 for oxygen (cathode). The inlet gas temperature and current load density were 550°C and 150 mA cm^{-2}, respectively. Only one of these parameters was changed in a certain range for each set of simulation results to see the effect of a specified parameter on the distribution of the stack temperature.

4.4. Effect of gas inlet temperature and external heaters

The effect of the temperature of the feed gas on the axial temperature distribution is analyzed in Fig. 8. Here, the main interest is how the inlet temperature change affects the overall temperature curves as well as the maximum temperature. The inlet gas temperature was varied from 450°C to 550°C with all other variables fixed. Though such a low temperature is not practical for MCFC operation, the simulation is intended to evaluate the effect of inlet gas temperature on stack temperature distribution. The change of gas inlet temperature influences the stack front temperature, and shifts the entire axial temperature profile almost in parallel. If we define a stack temperature rise as the temperature difference between the inlet and the maximum temperature, the temperature rise is almost invariant to the change of gas inlet temperature because of the parallel shift of temperature profiles. The maximum temperature, however, decreases as the inlet gas temperature drops due to the temperature shift. Such a drop in the

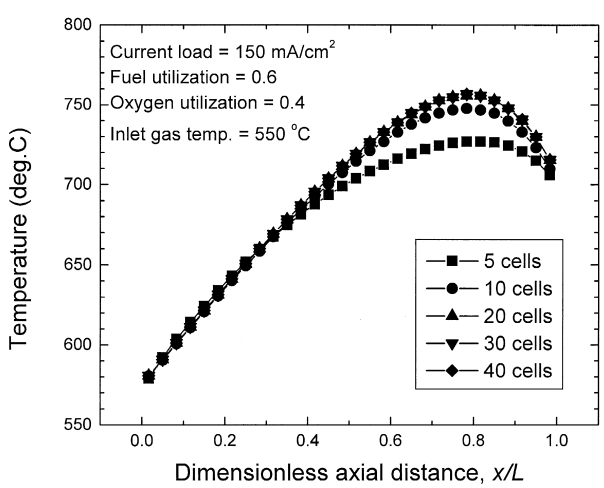

Fig. 7. Axial temperature profiles from numerical simulations for stacks with different numbers of cells.

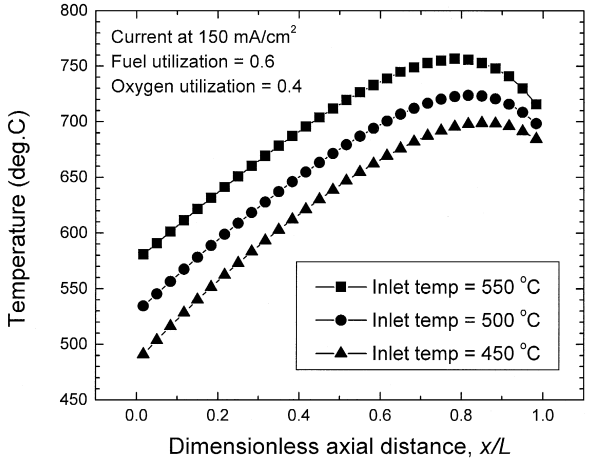

Fig. 8. Axial temperature profiles from numerical simulations at different inlet gas temperatures.

maximum temperature is obtained in return for sacrificing cell performance at the stack inlet since the low inlet temperature will drop the cell performance significantly. The lowest allowable temperature in a MCFC is higher than 500°C since the melting point of carbonate mixture is near 500°C for the given electrolyte composition. A decrease in inlet gas temperature exerts little beneficial effect on the overall stack temperature distribution and cell operation.

The top and bottom heaters are used to help the stack maintain a desired temperature, usually 650°C. The axial temperature profiles are compared in Fig. 9 when the heater temperature is lowered from 650°C to 600°C and then 550°C. If the heating plates have a large influence on the inside stack temperature rise, the maximum temperature should be reduced by lowering the heating temperature. The axial temperature profile does not change much except near the stack outlet, as shown in Fig. 9. The maximum temperature drops only a little even at the 550°C

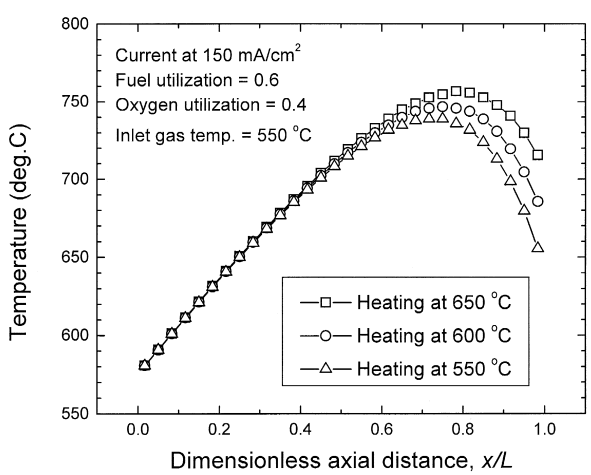

Fig. 9. Axial temperature profiles from numerical simulations at different stack heating temperatures.

heating temperatures. The external stack heaters have little influence on the inside of the stack. The effect of heating temperature may be illustrated better in vertical temperature profiles rather than in axial profiles. Vertical temperature profiles of the separator plates near the inlet and outlet of the stacks of Fig. 9, are presented in Fig. 10. The 41 separator plates for 40 cells are numbered on the ordinate from the lowest (zeroth) to the highest (40th), while temperature is plotted on the abscissa. The overall shapes of the vertical temperature profiles are similar to those reported by others [15]. The separators close to the upper and lower heaters (No. 0 and No. 40) preserve the temperatures of the heaters. In each case, the external heaters appear to influence about five cells from the top or bottom end walls. Beyond these cells the inside stack temperature is little influenced by stack heating. The inside temperature near the inlet is actually independent of heating temperature. The inside stack temperature near the outlet is slightly affected by the heating temperature, but the bulk of inside separators maintains a uniform temperature for each heating temperature. The outlet temperature profiles in Fig. 10 resemble oscillating curves which show an apex at the position of every five cells. As explained, this reflects the different thickness of the separator plates at these locations. The results of Fig. 10 also correspond to those of Fig. 7 where the stacks with 10 or more cells have an identical temperature distribution in the inside.

In Figs. 9 and 10, it can be been that the stack inside temperature is mostly affected by the heat of cell reactions rather than by the external heaters. The heaters at both vertical ends turn out to influence only a few cells. Though the stack heating temperature does not have much affect on the overall stack temperature distribution, the external heaters are considered to be essential elements of a stack

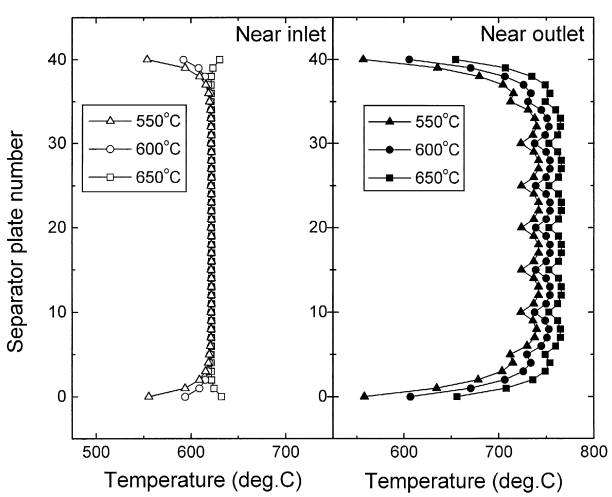

Fig. 10. Vertical temperature profiles from numerical simulations at different stack heating temperatures: fuel utilization = 0.6 and oxygen utilization = 0.4 at 150 mA cm^{-2} load with a gas inlet temperature of 550°C.

assembly to keep the cell temperature near the upper and lower walls close to the set point.

4.5. Effect of current load and gas utilization

In Figs. 8–10, the temperature conditions at stack boundaries (inlet gas and external heaters) were discussed in relation to how they change the inside temperature distribution curves of the stacks. The influence of the cell reactions on the stack temperature rise is shown in Fig. 11. Since the rates of the cell reactions are determined by the load current over the total cell area, the plot was made at different load current densities for the 40-cell stack. As most current–voltage curves indicate, the load current of an MCFC rarely exceeds 200 mA cm^{-2} and in most cases a current density of about 150 mA cm^{-2} is considered a base load. The axial temperature profiles in the current density range from 50 to 150 mA cm^{-2} are presented in Fig. 11. A low current load clearly results in a small temperature rise. Stable stack operation at atmospheric pressure is possible with a load below 75 mA cm^{-2} under the specified stack conditions in Fig. 11. Special consideration of stack cooling becomes necessary at a higher load operation. The result obviously shows that the cell reactions are the main source of thermal energy to raise the inside temperature of a large-scale stack. When MCFC stacks are configured with a heat-recovery system, a vast amount of the heat generated from cells at the base load is utilized for other turbine-based power-generation systems in a combined cycle. Stack cooling is therefore important not only to enhance the stack operation capability but also to increase the overall efficiency using combined cycle power generation.

We have shown so far the effect of parameters such as inlet temperature, heating power, and load current. These parameters define stack operation and more or less influence the stack inside temperature. Though managing those parameters is helpful for stack temperature control, they are not direct answers to the issue of stack cooling. A complete control of MCFC stack temperature is achieved by means of a cooling medium. There could be two kinds of sources for stack cooling medium: process gas and nonprocess gas or liquid. The use of coolant fluid that is not involved in the stack operation process has not been studied extensively, and it is not expected to draw much attention because of the unavailability of an efficient coolant under MCFC conditions and the need of another type of stack design for the coolant flow. The use of process gas as a coolant is now common for a large-scale stack operation. While the anode fuel gas is an expensive source that cannot be utilized in excess of the stoichiometric requirement, compressed air in the cathode gas can do double duty as a cathode reactant and a stack coolant. The effectiveness of cathode gas for stack cooling is well explained in Fig. 12 that shows the effect of cathode gas utilization on axial temperature profiles. It clearly demonstrates that cooling of the stack temperature can be achieved by increasing the cathode gas flow rate. The change of cathode gas flow rate significantly influences the maximum stack temperature and the overall temperature distribution. At a utilization of 0.2, the stack temperature is well maintained within the limit. Comparing the effects of other stack parameters shown so far, the use of excess cathode gas is undoubtedly the most influential in suppressing rise in the stack temperature.

The relationship between the stack maximum temperature and cell voltage and the cathode gas utilization is shown in Fig. 13. The cell voltage is an average for all the 40 cells. The fuel (anode) utilization is fixed at 0.6 while the oxygen utilization is varied from 0.6 to 0.2. No significant effect of cathode gas flow is found for the average cell voltage. The drop in the maximum temperature with

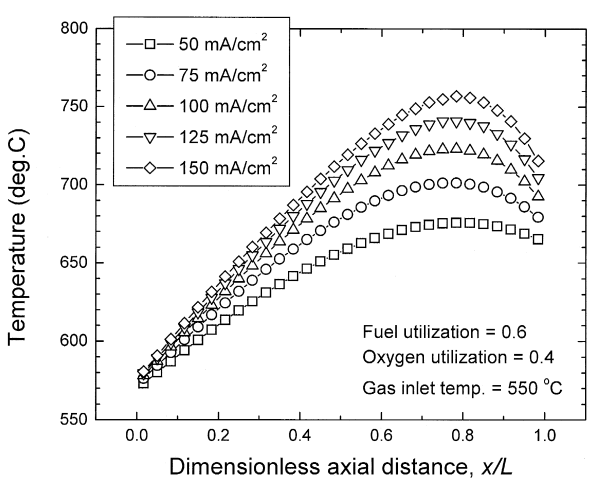

Fig. 11. Axial temperature profiles from numerical simulations at various current loads.

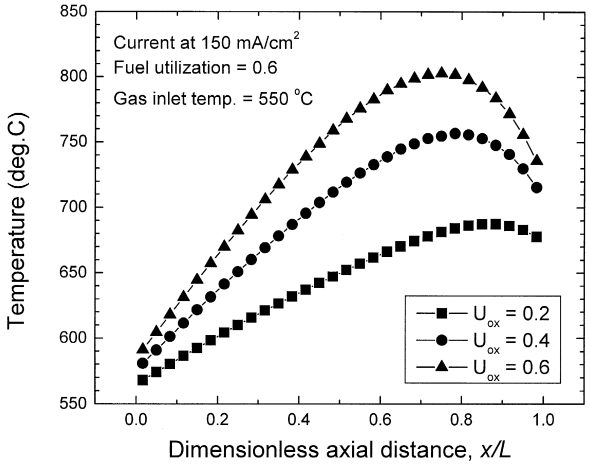

Fig. 12. Axial temperature profiles from numerical simulations at different cathode gas utilizations.

increase in the cathode gas flow (low gas utilization) is very dramatic. The total flow rate is inversely proportional to the gas utilization. A decrease in cathode gas utilization from 0.6 to 0.2 is equivalent to a threefold increase in the cathode gas flow rate. With this increase, the maximum temperature drops by more than 100°C.

The increase of cathode gas flow, however, causes another problem, as shown in Fig. 14, i.e., a serious increase in the pressure drop. In Fig. 14, the anode gas pressure drop is constant because the fuel utilization is not changed. The cathode gas pressure drop increases seriously as gas utilization decreases or the total flow rate increases. This pressure drop is a pressure difference between the inlet and outlet of each gas stream. In operation at atmospheric pressure, the outlet gas pressure is just above an atmosphere, and the outlet pressure difference between the anode and the cathode gases should be very low. The inlet pressure difference between the anode and the cathode gases, on the other hand, is estimated from each pressure drop, as shown in Fig. 14. For instance, the inlet pressure difference between anode and cathode is about 4500 Pa. MCFC stacks cannot tolerate such high gas pressures. Gas sealing in MCFC is maintained by a porous ceramic matrix impregnated with the liquid carbonate electrolyte. The anode and cathode gas flows create dynamic pressures and these pressures keep a balance within the bubble pressure barrier of the liquid electrolyte. The bubble pressure barrier is not so high that an increase of pressure difference between the two gas streams will break the balance and lead to gas leakage. The gas leakage results in the combustion reaction of hydrogen fuel with air and, consequently, a dramatic increase in local temperature. Pressure control is not a problem in a small-size cell, but is a critical issue in a large-scale stack. MCFC developers have already solved this problem by employing pressurized operation. A large-scale high-temperature fuel cell system with an external reformer expects to be operated at elevated pressures. Pressurized operation will reduce the gas pressure drop from increased residence time and slower gas velocity. A pressurized stack operation also promises an increase in cell performance as already reported by many researchers [3].

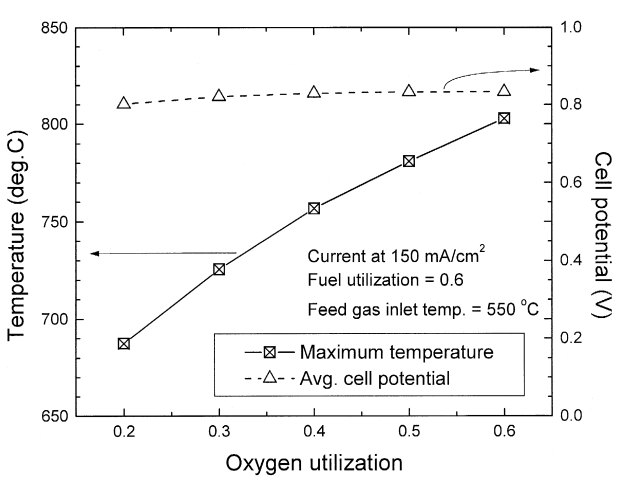

Fig. 13. Maximum stack temperature and average cell voltage as a function of cathode gas utilization.

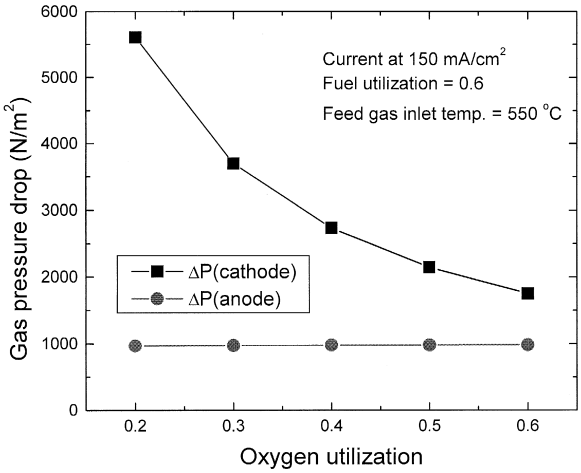

Fig. 14. Gas pressure drop as a function of cathode gas utilization.

5. Summary and conclusion

The proposed stack model is validated via temperature distribution compared with the measured data of a 5-kW test stack. A more significant temperature distribution is observed at a higher load, and its influence on nonuniform power density distribution is demonstrated. Further simulation results verify every aspect of the MCFC stack operation characteristics from the demonstration of axial temperature profiles at various stack parameters and operating conditions. A large effect of cell size on stack temperature rise is also clearly observed. The cell length has more influence on temperature rise than the number of cells. A change in the inlet gas temperature shifts the axial temperature distribution curves. The inlet gas temperature has no influence on the shape of axial temperature distribution, but it reduces the maximum temperature. The stack heaters located at the top- and bottom-end separator plates influence only a few cells from the end wall, and the inside temperature rise is mostly due to the heat released from the cell reactions. Increasing the cathode gas flow rate is the most effective in lowering the rise in stack temperature. All the simulation results corroborate the known fact that cathode gas is an efficient cooling medium and the stack temperature control is achieved with changing the cathode gas flow rate or utilization. The need for pressurized operation is addressed from the demonstrated results.

List of symbols

C	total molar concentration, mol m^{-3}
C_j	molar concentration of species j, mol m^{-3}
C_p	molar heat capacity or specific heat capacity, J $mol^{-1} \cdot K^{-1}$ or J $kg^{-1} \cdot K^{-1}$
D	diffusivity of gas, $m^2 s^{-1}$
E_{eq}	equilibrium cell potential, V
E^0	standard cell potential, V
F	(Faraday's constant) = 96 487 C mol^{-1}
H	stack height, m
ΔH	enthalpy change, J mol^{-1}
i	current density, mA cm^{-2} or A m^{-2}
K_{shift}	chemical equilibrium constant for the water–gas-shift reaction
k	thermal conductivity, W $m^{-1} \cdot K^{-1}$
L	cell length, m
m_j	volumetric mass source or sink of reactant/product species, kg $m^{-3} s^{-1}$
Q	rate of heat generation, W $m^{-3} K^{-1}$
R_{ohm}	ohmic resistance, $\Omega \cdot m^2$
r_j	chemical or electrochemical reaction rate for species j, mol/m^2 s or mol/m^3 s
u	velocity vector $[u_x, u_y, u_z]$, m s^{-1}
U_f	fuel utilization in anode
U_{ox}	oxygen utilization in cathode
W	cell width, m
V_{cell}	cell potential under electrical load, V
y_j	mole fraction of species j
z_j	number of electrons transferred in the reaction for each species j

Greek letters

δ_{cell}	cell thickness, m
δ_g	gas channel height, m
μ	viscosity, kg m^{-1} s^{-1}
ρ	density, kg m^{-3}
η	impedance for electrode overpotential, $\Omega \cdot m^2$

Acknowledgements

This work was carried out within the project titled "Development of a 100-kW externally reforming MCFC system" and was supported by the Korea Electric Power Corp. and the R&D Management Center for Energy and Resources of The Korea Energy Management Corp. We thank Samsung Heavy Industries for providing stack components for the 5-kW stack test.

References

[1] J.H. Hirschenhofer, D.B. Stauffer, R.R. Engleman, Fuel Cells — A Handbook (Revision 3), prepared by Gilbert/Commonwealth for the U.S. Department of Energy under Contract No. DE-AC01-88FE61684, January 1994.
[2] M. Matsumura, T. Shinoki, T. Yagi, JSME Int. J. 41 (1998) 691–696.
[3] L.J.M.J. Blomen, M.N. Mugerwa (Eds.), Fuel Cell Systems Plenum, New York, 1993.
[4] M. Yoshikawa, Y. Mugikura, T. Watanabe, T. Ota, A. Suzuki, J. Electrochem. Soc. 146 (1999) 2834–2840.
[5] N. Kobayashi, H. Fujimura, K. Ohtsuka, JSME Int. J. 32 (1989) 420–427.
[6] H. Fujimura, N. Kobayashi, K. Ohtsuka, JSME Int. J. 35 (1992) 82–88.
[7] W. He, Q. Chen, J. Power Sources 55 (1995) 25–32.
[8] F. Yoshiba, N. Ono, Y. Izaki, T. Watanabe, T. Abe, J. Power Sources 71 (1998) 328–336.
[9] C.Y. Yuh, J.R. Selman, J. Electrochem. Soc. 138 (1991) 3642–3648.
[10] S.V. Patankar, Numerical Heat Transfer and Fluid Flow, Hemisphere, New York, 1980.
[11] R.C. Reid, J.M. Prausnitz, T.K. Sherwood, The Properties of Gases and Liquids, 3rd edn., McGraw-Hill, New York, 1977.
[12] J.-H. Koh, B.S. Kang, H.C. Lim, AIChE J, submitted for publication.
[13] S. Takashima, K. Ohtsuka, N. Kobayashi, H. Fujimura, Proc. of the 2nd Electrochem. Soc. Symp. on Molten Carbonate Fuel Cell Technology, October, Seattle, WA, USA, 1990, pp. 378–394.
[14] N. Zaima, Proc. of the Symp. on Fuel Cells, November 6–7, San Francisco, CA, USA, 1989, pp. 147–159.
[15] T. Matsuyama, A. Matsunaga, T. Oagawa, Proc. of the 4th Int. Symp. on Carbonate Fuel Cell Technology, Montreal, Canada, 1997, pp. 167–178.